International Journal of Mass Spectrometry 287 (2009) 46–57

Contents lists available at ScienceDirect

International Journal of Mass Spectrometry

journal homepage: www.elsevier.com/locate/ijms

# A new, higher resolution, ion mobility mass spectrometer

Paul R. Kemper, Nicholas F. Dupuis, Michael T. Bowers*

*Department of Chemistry and Biochemistry, University of Calif. at Santa Barbara, Santa Barbara, CA 93106-9510, United States*

ARTICLE INFO

*Article history:*
Received 17 September 2008
Received in revised form 13 January 2009
Accepted 21 January 2009
Available online 31 January 2009

*Keywords:*
Ion mobility
MALDI
Electrospray
Ion funnel
Collision cross section

ABSTRACT

Ion mobility spectroscopy (IMS) coupled with mass spectrometry (MS) has become a key tool for investigation of molecular conformation and aggregation. The technique has been widely applied to both biological and inorganic materials. The ability to distinguish isomers with similar shapes (and cross sections) is the critical advantage of IMS. Of equal importance is the ability to distinguish different oligomer states with the same value of $m/z$ (singly charged monomer, doubly charged dimer, etc.). We present here a combined IMS–MS instrument able to resolve structures with cross sections differing by less than 1%. Ions can be produced either by electrospray or MALDI ionization. Ion funnels are used at both the entrance and exit of a 2 m long drift tube. Mass analysis can be done either with a quadrupole or TOF mass spectrometry following the drift tube. The use of a quadrupole mass spectrometer provides very high sensitivity although the mass range is limited. A variety of experiments and applications to several previously studied chemical systems and standard peptides are presented. These include both ESI and MALDI mass spectrums, high resolution ion mobility experiments and identification of oligomeric state through mobility selected mass spectrometry.

## 1. Introduction

Ion mobility mass spectrometry (IMS) is an old technique which has seen an enormous renaissance in the last 15 years [1–5]. Its ability to distinguish molecules of different structure and the same mass has given it increasing importance. Coupled with molecular structure calculations [6] and the accompanying cross section calculation [3b,7], IMS cross section measurements can give unique insight into the structures present in a given molecular system. The technique has been applied to a wide variety of such systems including ligated metal clusters [8], synthetic polymers [3b,6b,9], oligonucleotides [10] as well as peptides and proteins [11].

A number of different forms and permutations of IMS have been developed. In addition to the basic high-pressure drift tube, techniques such as FAIMS [12], a segmented quadrupole drift cell [13] and a transient wave ion guide have been described [14]; all adding a degree of structural separation to a mass spectrometric technique. Further, the addition of time of flight mass spectrometry (TOFMS) to IMS has been widely implemented and used [15–17]. The instrument recently described by Baker et al. [17] is an especially sophisticated example incorporating a high pressure, high resolution drift tube. More specialized techniques such as multistage IMS (IMS–IMS) has also been described [18]. It is worth noting that much of this instrumentation has been made possible through the development of the ion funnel which turns the inherently very low transmission drift tube into a high sensitivity analyzer [19–22].

The predominant thrust in much of this instrumental development has been the development of the scanning techniques needed to rapidly and easily determine the components in unknown, complex mixtures (see Ref. [17] and the references therein). Our experimental thrust has been more towards the coupling of accurate absolute cross section measurements with molecular structure calculations to determine structures of known compounds [5–7]. Towards that goal, higher resolution measurements allow us to resolve the multiple stable structures which may be hidden under a single, less well resolved, IMS peak.

We present here a new IMS instrument capable of separating molecules with cross sections which are less than 1% different. Ions can be formed either by MALDI or electrospray ionization. In addition, the instrument can mass analyze individual IMS peaks with either TOF or quadrupole mass spectrometers (QMS). Finally, the drift tube has been designed to be cooled with the aim of both increasing IMS resolution and freezing out inter-converting molecular structures.

The paper will first discuss the separate parts of the instrument, then the possible experiments and finally some applications to chemical systems which illustrate the instrument's abilities.

## 2. The instrument

An overview of the instrument is shown in Fig. 1. Beginning with the source region, the sections are discussed in order from left to right.

---

* Corresponding author.
*E-mail address:* ijms@chem.ucsb.edu (M.T. Bowers).

1387-3806/$ – see front matter © 2009 Elsevier B.V. All rights reserved.
doi:10.1016/j.ijms.2009.01.012

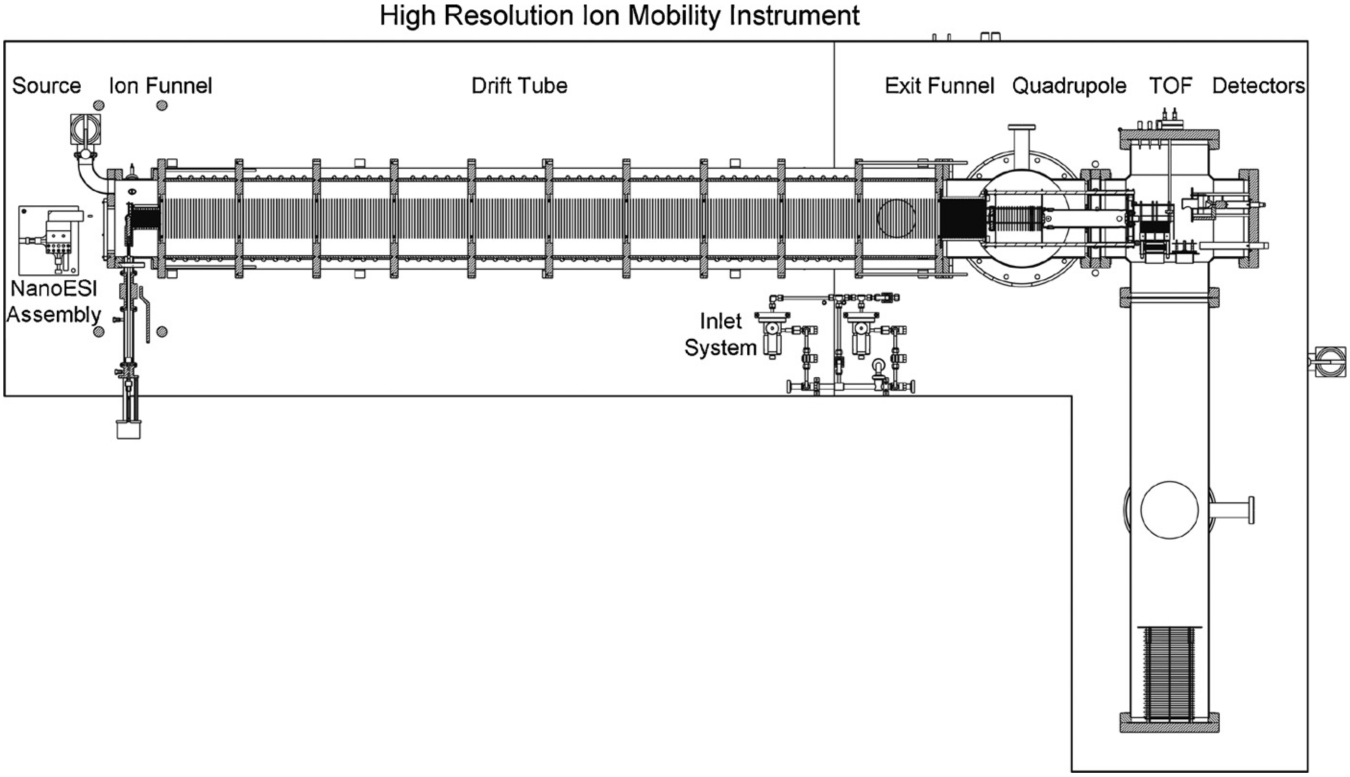

**Fig. 1.** Overview of the instrument. The length of the drift tube is 2.00 m. The drawing is to scale.

### 2.1. Ion source

The instrument is equipped with both Electro/Nano spray and MALDI ion sources. A schematic view is shown in Fig. 2. Changing between the two types of sources requires venting with helium and switching one external plate. Subsequent pump down to a useable pressure requires about 1.5 h.

#### 2.1.1. Nanospray ESI source

The metalized glass pico-tip sample holder is held in a xyz translation stage and biased at 900–1400 V with respect to the capillary (Fig. 1). The capillary (75 mm long × 0.25 mm I.D.) is held in a heatable aluminum block (usually held at 300 K) and extends to the first ring of the entrance ion funnel shown in Fig. 2. The capillary can be biased slightly negative (0 to −10 V) with respect to the

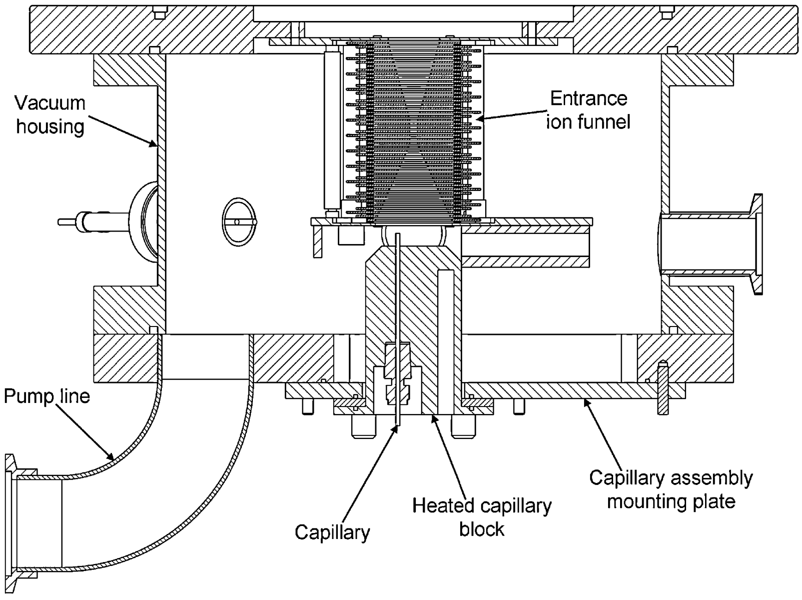

**Fig. 2.** Detailed view of ESI source region.

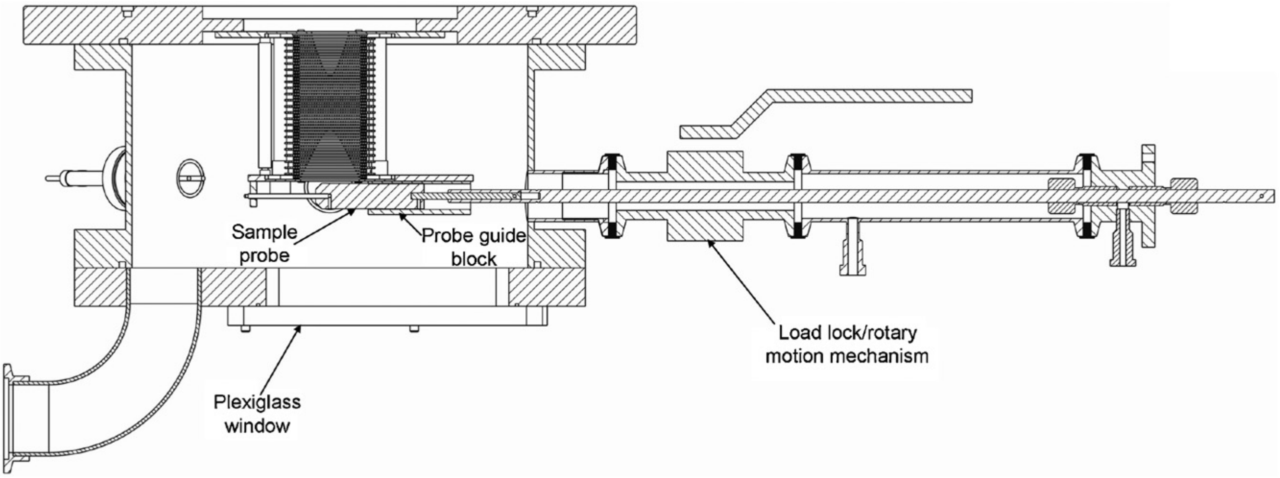

**Fig. 3.** Detailed view of MALDI source region.

funnel entrance in positive ion mode. This may be counter intuitive (as one might expect the ions to be pulled away from the funnel) but it can result in a 10–20% increase in signal. No flow disrupter [23] is used and instead the capillary is offset from centerline [20].

### 2.1.2. MALDI source

When using the MALDI source the ESI capillary block is removed and replaced with a Plexiglas window to allow the probe position to be viewed (Fig. 3). This, in turn, allows easy alignment of the probe and greatly facilitates sample loading. Samples are coated on a 12 mm diameter × 30 mm long cylindrical probe. The probe is rotated externally with a 6.25 mm rod and rotary motion feed through (Fig. 1). A threaded rod in the nose of the probe engages the source and provides linear translation as the probe rotates. A relatively large surface area of sample is required for the long sample lifetimes required in the IMS/MS experiments. The present arrangement provides about 2 h of sample lifetime without reloading the sample. A diode pumped YAG laser operating at 355 nm (Lumanova Flare [24]; Model 200–100; 100 μJ, 200 Hz) is used to irradiate the sample. The beam is attenuated using a polarization rotator and beam splitter. This is a critical adjustment which greatly impacts the intensity of analyte ions generated. A 150 mm lens focuses the vertical beam onto the sample probe through a quartz window on top of the source chamber. Optimal signal intensity is obtained with the beam just skimming the probe. This position is set using a second window in the bottom of the source chamber where the laser light which passes the probe exits the chamber.

Due to the relatively high pressure in the ion source chamber (12–15 Torr, typically), desorbed ions and neutral molecules are cooled and trapped near the probe. This can result in ion-neutral and clustering reactions usually leading to sample plus matrix adduct peaks. The result is a generally “noisier” mass spectrum compared with that obtained with low pressure MALDI.

### 2.1.3. Ion funnel

The source ion funnel has the general hourglass shape first described by Tang et al. [21] and subsequently modified for use at higher pressures [17]. It consists of a total of 47 plates (0.75 mm thick) separated by Teflon (PTFE) rings (also 0.75 mm thick). The first section (20 plates) tapers from 30 mm diameter to 3.2 mm diameter The second section (7 plates) has a constant 3.2 mm diameter and serves as the differential pressure aperture (see below). The diameter of the third section (20 plates) increases from 3.2 mm to 20 mm in diameter and forms the ion trap volume. The increase in volume (relative to a continuation of the 3.2 mm section) helps reduce coulomb repulsion between the stored ions and should reduce ion loss in the trap. SIMION [25] simulations of the trap behavior show the ions clustering in a torus near the large end of the trap. RF trap voltages are uniform throughout the trap and are typically 40–100 $V_p$ at 1.3 MHz. Initially, a constant-value resistor chain provided a uniform DC voltage drop from plate to plate through all 47 plates. This uniform field is not optimal and variable resistor bypasses have been added to the second and third sections (3.2 mm section and trapping section) to allow the DC field to be varied from 0 to 100% of the maximum value set by the total voltage applied to the funnel. At present typical DC fields are ∼16 V/cm. The adjustable field in the trapping section of the ion funnel allows optimization of the ion trapping leading to a 20% increase in trapped ion intensity at ∼80% of the DC voltage value. The last plate of the funnel is the ion gate. It is screened and has a DC voltage only. Typically, a blocking voltage of 15–30 V (above the “transmit” voltage) is applied to trap the ions. “Gate Open” pulse widths of at least 80 μs are required to move the ions from the trap into the drift tube. This is far longer than what the SIMION simulations require and the origin of the discrepancy is unclear. Following the trap is a 6 mm space before the drift tube entrance plate (also screened). This is to prevent RF and/or gate pulse penetration into the drift tube and give a precisely defined start for the drift length and the drift potential.

### 2.1.4. Pumping and gas flow

In order to prevent unwanted neutral molecules from entering the drift tube a small flow of helium buffer gas is maintained from the drift tube through the entrance funnel and into the source chamber. The counter flow is produced by precisely maintaining the source chamber pressure at ∼0.08 to 0.20 Torr below the drift tube pressure. In practice, this is done by pumping constantly on the source at ∼5 l/s with a rough pump and adjusting a separate flow of helium into the source chamber to maintain the desired pressure differential. A differential capacitance manometer/control valve loop is used to set the helium flow into the source (helium flow into the drift tube is set separately). The partial pressures of $N_2$ and $H_2O$ are monitored with a residual gas analyzer (RGA) in the low pressure chamber following the drift tube and the differential pressure across the entrance funnel is adjusted to keep these contaminants <500 ppm of the helium buffer gas.

## 2.2. The drift tube

The present tube has a total drift length of 2.00 m. The outer vacuum chamber consists of 10 equal length sections made of 200 mm

O.D. stainless steel tubing separated by 300 mm O.D. × 19 mm thick glass filled PEEK (polyetheretherketone) insulating flanges. O-ring seals are used throughout to seal the sections together. A linear drift field is maintained with a series of 290 stainless steel rings (100 mm O.D. × 75 mm I.D.) connected by 100 kohm precision resistors. The rings are stacked in 10 individual sections on 3.18 mm ceramic rods separated by precision cut Pyrex spacers (6.35 mm long). The first and last drift rings are screened (90% transmission) to provide a well defined length and linear drift field. The external chamber sections are biased with a separate resistor chain to prevent arcing between the chamber wall and the drift rings. The potential between the ion source funnel exit and the drift tube entrance can be adjusted from 0 to 100 V. In practice, all ions are injected into the drift tube at ∼10 V and higher voltages have no effect on ion signal. Either nitrogen or helium can be used in the tube however in practice almost all experiments done to date have been with helium. Easier parameterization in cross section calculations makes helium the gas of choice for our experiments. We also observe slightly better resolution with helium than nitrogen (∼110 in He compared to 100 in $N_2$). The reason for this better resolution with helium is unclear since there is no theoretical dependence on bath gas species. We attribute this discrepancy to the design parameters of the instrument which do not allow application of high enough drift and funnel voltages with nitrogen to achieve the best resolution. Ion transmission (sensitivity) also appears to be greatly reduced when using nitrogen bath gas. Improved transmission in $N_2$ requires high exit funnel RF and DC voltages leading to the arcing problems that limit application high drift voltages thus limiting optimal resolution. Electrical discharge problems are greatly reduced by the relatively high pressure of helium used (typically 12–15 Torr) but if necessary, a small pressure of $SF_6$ (<0.5%) can be introduced to completely prevent discharging. This is not necessary for routine mobility measurements which do not require the highest tube voltages but can be useful for high resolution experiments. The tube pressure is set with a manual leak valve and measured with a second precision capacitance manometer. To clean up the tube and prevent oil back streaming, a small turbo pump (200 l/s) is fitted and runs when the tube is not filled with gas. The tube is designed to be run with a maximum of 10 kV of drift voltage. In practice the best resolution (in He) is obtained with drift voltages between 4 and 5 kV. This is discussed below.

The drift tube is also designed to be cooled. To accomplish this, each stainless steel outer section is wrapped (externally) with 9.5 mm copper tubing which is welded to the stainless steel tube. The assembly is insulated with 3 layers of 12.5 mm thick closed cell foam and shrouded with warm, dry nitrogen. To prevent condensation build up on the cooled sections and connections, which leads to electrical leakage and loss of drift voltage it is necessary to completely isolate the cooling connections for each section. Temperatures of the individual sections are monitored by insulated thermocouples inserted in grease filled wells welded to the outside of the sections. Differential expansion occurs in both transverse and longitudinal directions. It occurs between the stainless steel outer chamber and the PEEK flanges as well as between the PEEK flanges and the drift ring assemblies. To accommodate the transverse expansion/contraction, the six mounting holes in the plastic flanges which contain the ceramic rods of the drift ring assemblies, are elongated radially. This provides precise location of the assemblies while allowing the flange to contract and expand. To accommodate the longitudinal movement, the PEEK flanges ride on two 25.4 mm ground rods, allowing free lengthwise expansion. To date the drift tube has been cooled to ∼−30 °C at which point further cooling is inhibited by leaks in the drift tube due to the differential expansion across the o-ring seals. Problems due to condensation have been eliminated with the insulation and shrouding described above but the vacuum failure will probably require extensive reengineering.

### 2.3. Exit funnel

The exit funnel (Fig. 4) is of conventional design [17,18]. It tapers from a 75 mm I.D. (equal to the drift tube I.D.) down to a 0.5 mm exit

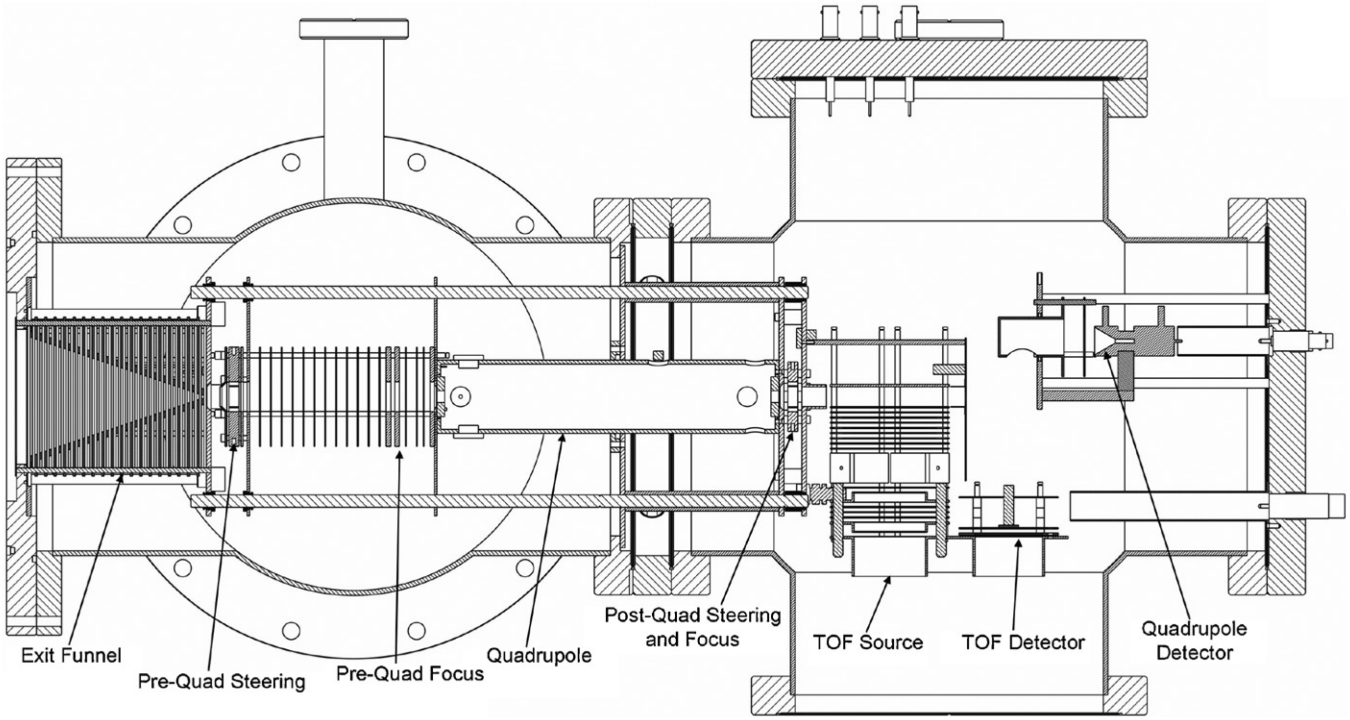

**Fig. 4.** Detailed view of the Quadrupole/TOF/Detector region.

orifice over a length of 114 mm. Stainless steel rings (37 pcs, 1.5 mm thick) alternate with PTFE spacers (38 pcs, 1.5 mm thick). Because the exit orifice (of the funnel) is the differential pressure aperture between the tube and the next chamber, the funnel sections must be as gas tight as possible and the PTFE spacers were lightly coated with high vacuum (Fombolin) grease. The entire assembly is clamped to help ensure a good seal. The gas flow out of the tube is actually less than anticipated, indicating the approach was successful. Excess material was removed from alternate lenses to reduce the device capacitance.

The total DC voltage across the funnel is 80–120 V with RF voltages of 75–90 $V_p$ at 1.3 MHz. The transmission of the drift tube and exit funnel combination is excellent. The only major losses occur below ∼1600 V where the ion packet begins to interact with the drift tube electrodes before reaching the exit ion funnel. Above ∼1600 V the ion current is independent of drift voltage indicating that all the ions entering the drift tube are collected and transmitted by the exit ion funnel. Transmission through the 0.5 mm exit orifice is almost entirely hydrodynamic (according to SIMION simulations) and it is possible that this orifice could be reduced to allow even greater pressure in the drift tube.

### 2.4. Quadrupole and transfer lens

This section of the instrument is detailed in Fig. 4. Upon leaving the exit funnel the ions enter a three element lens which focuses the ions and sets their energy as they enter the quadrupole. A xy steering element is incorporated near the start of the focusing lens. In addition to maximizing transmission the steering lens is used to select a particular ATD feature for quadrupole mass analysis (discussed below). To record an arrival time distribution (ATD), ion energies entering the quadrupole are typically set at 40 eV for optimal transmission and sensitivity and to reduce the time the ions spend outside the drift tube. For optimal quadrupole resolution, ion energies of 10–15 eV are used. The quadrupole is a 4000 amu unit (Extrel Core MS [26]) and forms the differential pumping aperture between the transfer lens and TOF chambers.

The transfer lens chamber is pumped with a 250 mm diffusion pump and the typical pressure while running is $\sim 5 \times 10^{-4}$ Torr. A diffusion pump was chosen for this chamber, rather than a turbo pump, for the high He pumping speed (∼3500 l/s). A residual gas analyzer is fitted to this chamber and is used to monitor unwanted diffusion into the drift tube from the source as well as the partial pressure of $SF_6$ if used.

### 2.5. TOFMS and detectors

Upon exiting the quadrupole the ions pass through a second focus/steering combination lens and enter the TOF source (Fig. 4). If the TOF source is not pulsed, the ions transit the source and are detected with a conversion dynode and electron multiplier. The resulting quadrupole mass scans and arrival time distributions are collected on an Ortec multi-channel scalar board (Ortec MCS Plus [27], 100 ns resolution). If the TOF source is pulsed, the ions present in the source volume (∼35 mm diameter) are pushed out, through a grid, with a fast (15 ns rise time), variable height, pusher pulse. The ions then enter a linear acceleration region with a constant 9 kV acceleration potential. The pusher/acceleration sections form a Wiley-McLaren source. After a 1 m, field free section the ions enter a single stage reflectron and are returned to the microchannel plate detector (50 mm diameter chevron). The front surface of the channel plate is maintained at the acceleration/field-free region potential. The anode (biased at high voltage) is coupled to the input (virtual ground) of a fast preamp (Ortec VT120 [27]) with a 500 pf capacitor. The resulting pulsed output is collected with a fast MCS board (Ortec 9353 [27], 100 ps resolution). Both detectors can be operated simultaneously allowing an ATD to be collected along with a TOF mass spectrum of one of its components. This is a unique ability and is illustrated below.

The TOF/detector section of the instrument is pumped with a 160 mm diffusion pump (700 l/s He pumping speed) and has a normal base pressure of $\sim 4 \times 10^{-9}$ Torr. During operation the pressure rises to $\sim 5 \times 10^{-7}$ Torr. This is high enough to cause collisional broadening of the TOF spectra and more pumping is needed here.

### 2.6. Inlet system

A separate, diffusion pumped, vacuum system is used to evacuate inlet lines, the MALDI probe load lock and to set pressures in the tube (Fig. 1). The two leak valves allow easy switching between He and $N_2$ bath gasses and the introduction of $SF_6$ (when used).

### 2.7. Electronics

The control/drift electronics are conventional, consisting of power supply modules floated at the output potential of the previous stage. This provides more stable outputs than a control loop system with the modules referenced to ground. The RF power supplies for the funnels are described in the literature [28]. The source funnel supply is coupled to the funnel (biased at up to the 10 kV drift voltage) with HV isolation capacitors. These RF supplies are tuned circuit oscillators and, in order to operate with a reasonable Q factor at the 800–1200 kHz desired, the funnel capacitance must be minimal. The present funnels have capacitances of ∼1200 pf and oscillate at ∼1.3 MHz. The maximum voltage out is ∼400 $V_p$ (peak to peak) with a 250 VDC input. This is sufficient to cause discharging and thus more than adequate for the experiment. No attempt has been made to optimize the funnel frequencies.

## 3. Experiments and performance

In this section we detail the various experiments possible on the instrument and the resulting performance. For the experiments discussed below all peptide samples (Bradykinin, Angiotensin II, Leucine Enkephalin derivatives and GRGDS/SDGRG) were purchased from Sigma (St. Louis, MO) and used without further purification. Sample stock solutions were prepared in 50:50, MeOH:$H_2O$ (HPLC grade) at ∼1 mg/ml and either used directly or diluted to for optimal ion intensity. Samples for electrospray experiments were loaded in gold coated borosilicate capillaries pulled to a fine point on a tip puller (Sutter Instrument Co., Novato, CA). For MALDI sample preparation the same analyte stock solutions were used. Matrix solutions were made of 2,5-dihydroxybenzoic acid in MeOH (HPLC grade) at a concentration of 100 mg/ml. The matrix and analyte solutions were mixed in a 10:1 ratio and ∼50 μl of this solution was applied to the sample probe.

### 3.1. Quadrupole mass spectrum

A simple ESI quadrupole mass scan (no source pulsing) of bradykinin [RPPGFSPFR] is shown in Fig. 5. The mass resolution here is >1000 with the 0.5 amu $^{13}C$ spacing of the $(BK+2H)^{+2}$ ion ($m/z = 531$) clearly resolved.

### 3.2. Arrival time distributions

A high resolution ATD of the +2 peak of angiotensin II [NRVYIHPF] is shown in Fig. 6(a) ($m/z = 523.09$). The ESI source was used. The measured drift time to peak width (FWHM) ratio ($t_a/\Delta t$) is 109. This is certainly one useful measure of the instruments resolution.

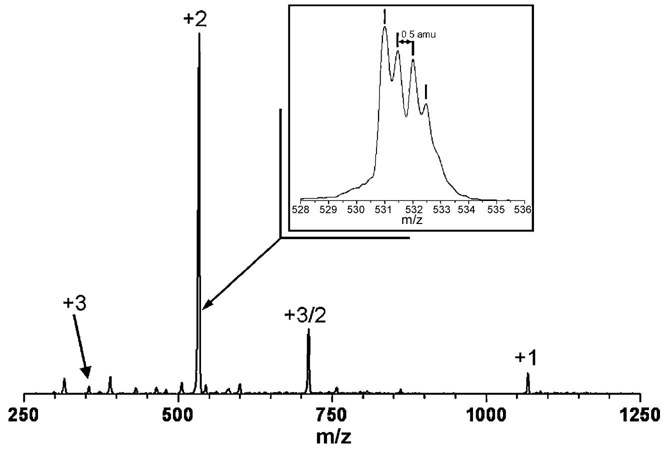

**Fig. 5.** Quadrupole mass scan of bradykinin formed by ESI. The inset shows a blow up of the +2 charge state peak where the 0.5 *m/z* spacing indicates this peak is a +2 monomer.

Another way to demonstrate resolving power is to simultaneously measure two ATD peaks with a known separation. In practice, it would probably be impossible to find two species with a ~1% difference in cross section where that difference was sufficiently well defined. An alternative is to measure the same ATD peak at two drift fields different by 1%. Since the difference in drift potentials is easily measured to 0.01%, the apparent difference in mobilities is accurately determined. Such an experiment is shown in Fig. 6(b). The ATD was first recorded at a drift voltage of 4940 V; the voltage was increased to 4990 V and the data collection was continued and added to the existing spectrum. This should accurately simulate the ATD spectrum that would result from a 50–50 mix of species whose mobilities differed by 1.01%. It is clear from the ~50% valley that the present instrument can easily resolve species whose cross sections differ by ~1%.

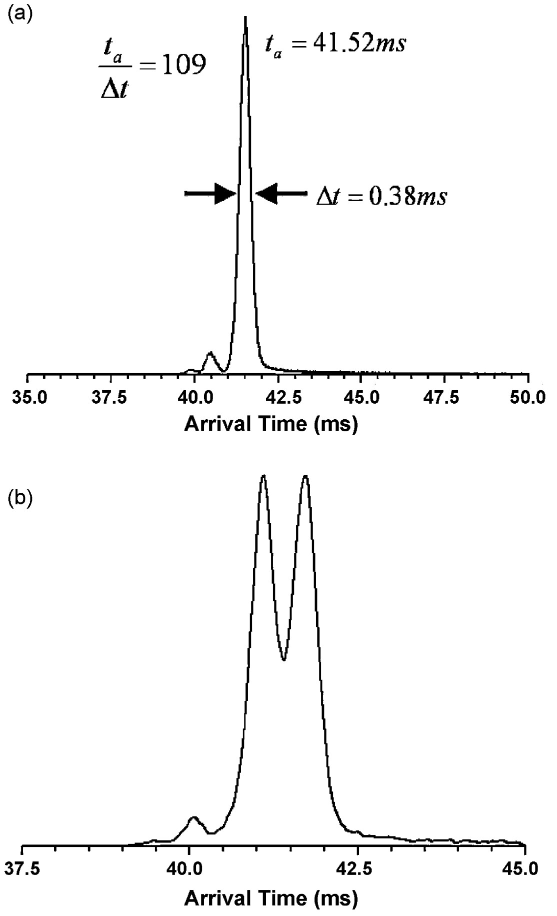

**Fig. 6.** (a) Arrival time distribution of angiotensin II +2 charge state showing an IMS resolution = 109; (b) the same ATD recorded at drift voltages of 4990 and 4940 with the spectra superimposed. This result shows that an experimental ATD of a mixture of two ions with mobilities 1.01% different will be resolved with a 50% valley.

The resolving power of the drift tube alone is given by [29]

$$\frac{t_{\mathrm{d}}}{t_{1/2}} = \frac{1}{4}\left[\frac{q}{k_{\mathrm{b}}\ln 2}\right]^{1/2}\left[\frac{V_{\mathrm{d}}}{T}\right]^{1/2} \tag{1}$$

where $t_{\mathrm{d}}$ is the drift time, $t_{1/2}$ is the width of the peak at half-height, $q$ is the charge of the ion, $V_{\mathrm{d}}$ is the voltage drop across the drift cell, $k_{\mathrm{b}}$ is Boltzmann's constant and $T$ is the temperature of the bath gas. In fact, the highest ATD resolution does not come at the highest drift voltage. This was noted by Hill and coworkers [30] and discussed by Baker et al. [17] and is due to the ATD time spread that occurs outside the drift tube (due to finite injection pulse width as well as the time spread created in both the exit funnel and (to a small extent) in the quadrupole and detector). Low drift fields (long times) minimize these "external" effects but give wide peaks due to longitudinal diffusion in the drift tube. High fields reverse the relative importance. The best resolution is found at some intermediate voltage; in the present instrument a drift voltage of 4–5 kV is optimal. The time spread added in the exit funnel appears to be the most significant external effect in this instrument (not the injection pulse width) and high drift fields in the funnel are required for the best resolution.

Finally, it should be noted that high resolution MALDI ATD experiments are problematic due to difficulty in trapping the ions in the source funnel. The problem appears to be ion loss due to coulomb repulsion due to the large instantaneous ion fluxes. This is probably due to the very large flux of matrix ions. When a single species is present (as in the $C_{60}$ laser desorption experiments), the MALDI ions are easily trapped and high resolution is routine.

### 3.3. Mobility measurements

Ions formed by ESI are trapped and gated in the source funnel; when using the MALDI source, the pulsed laser effectively gates the ions. In both cases, reduced mobilities ($K_0$) are measured by plotting arrival time ($t_{\mathrm{a}}$) vs. $P/V_{\mathrm{d}}$, where $P$ is the pressure in the drift tube $V_{\mathrm{d}}$ is the voltage across the drift tube. The relationship is shown in Eq. (2),

$$t_{\mathrm{a}} = t_{\mathrm{d}} + t_0 = \frac{l^2}{K_0}\frac{273.16}{760T}\frac{P}{V_{\mathrm{d}}} + t_0 \tag{2}$$

where $T$ is the bath gas temperature, $l$ is the drift tube length and $t_0$ is the (constant) time outside the drift tube for ions of a particular $m/z$ and mobility. The resulting slope is inversely proportional to reduced mobility and the intercept is equal to $t_0$. An example is shown in Fig. 7 for the +2 charge state of angiotensin II. These plots are extremely linear, indicating that "second order" effects in the exit funnel are unimportant. These small effects arise because the ion's drift time in the exit funnel is somewhat dependent on the drift tube voltage. This, in turn, is because the extent of transverse diffusion in the tube increases with lower drift voltages and the average displacement of the ions off center upon entering the funnel also increases. This results in a longer trajectory in the funnel and a longer apparent drift time. Thus, lower drift voltages increase both the tube drift time and the time in the exit funnel. The end result is an apparent increase in the slope of the arrival time vs. $P/V_{\mathrm{d}}$

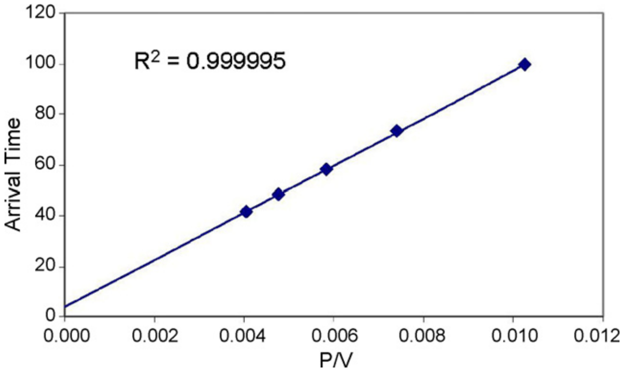

**Fig. 7.** Plot of arrival time vs. drift voltage/pressure for the angiotensin II +2 ion (see Eq. (2)). Note the high degree of linearity.

plot and an erroneously small mobility. If extremely low fields are used in the exit funnel, this effect is accentuated to the point that the mobility plots do become measurably non-linear. This non-linearity is predicted by SIMION trajectory simulations.

As a final check on the reliability of the mobility measurements, a number of previously determined mobility values were remeasured with the present apparatus. As shown in Table 1, excellent agreement was found in all cases.

**Table 1**

Comparison of mobilities measured on new high resolution instrument with previously published values.

| System | This work $K_0$ (cm$^2$/Vs) | Literature $K_0$ (cm$^2$/Vs) |
|---|---|---|
| $Cs^+$ | 18.13 ± 0.3 | 18.3 ± 0.3[a] |
| $C_{60}^{+}$ | 4.27 ± 0.08 | 4.32 ± 0.041[b] |
| $Bradykinin^{2+}$ | 4.45 ± 0.08 | 4.42 ± 0.08[c] |

[a] Ref. [34].

[b] Ref. [35].

[c] Refs. [20], [32d].

### 3.4. TOF mass spectra

A common reason to add TOFMS capability to IMS is to provide *m*/*z* data for a 2D cross section vs. *m*/*z* plot. In this application, the TOF source is pulsed at a rate of 5–10 kHz (not synchronized with the source gate pulses) and TOF data are collected continuously. In the present instrument, the TOFMS allows determination of oligomer numbers using the $^{13}$C spacing. In this application, the TOF sampling is coordinated with the IMS arrival time such that the TOFMS is collected of a single ATD feature. Although the non-synchronized experiment described above provides the same data, the present experiment has the advantage of simplicity and greatly reduced data acquisition and handling requirements. There is an additional advantage in terms of TOF signal intensity, being that

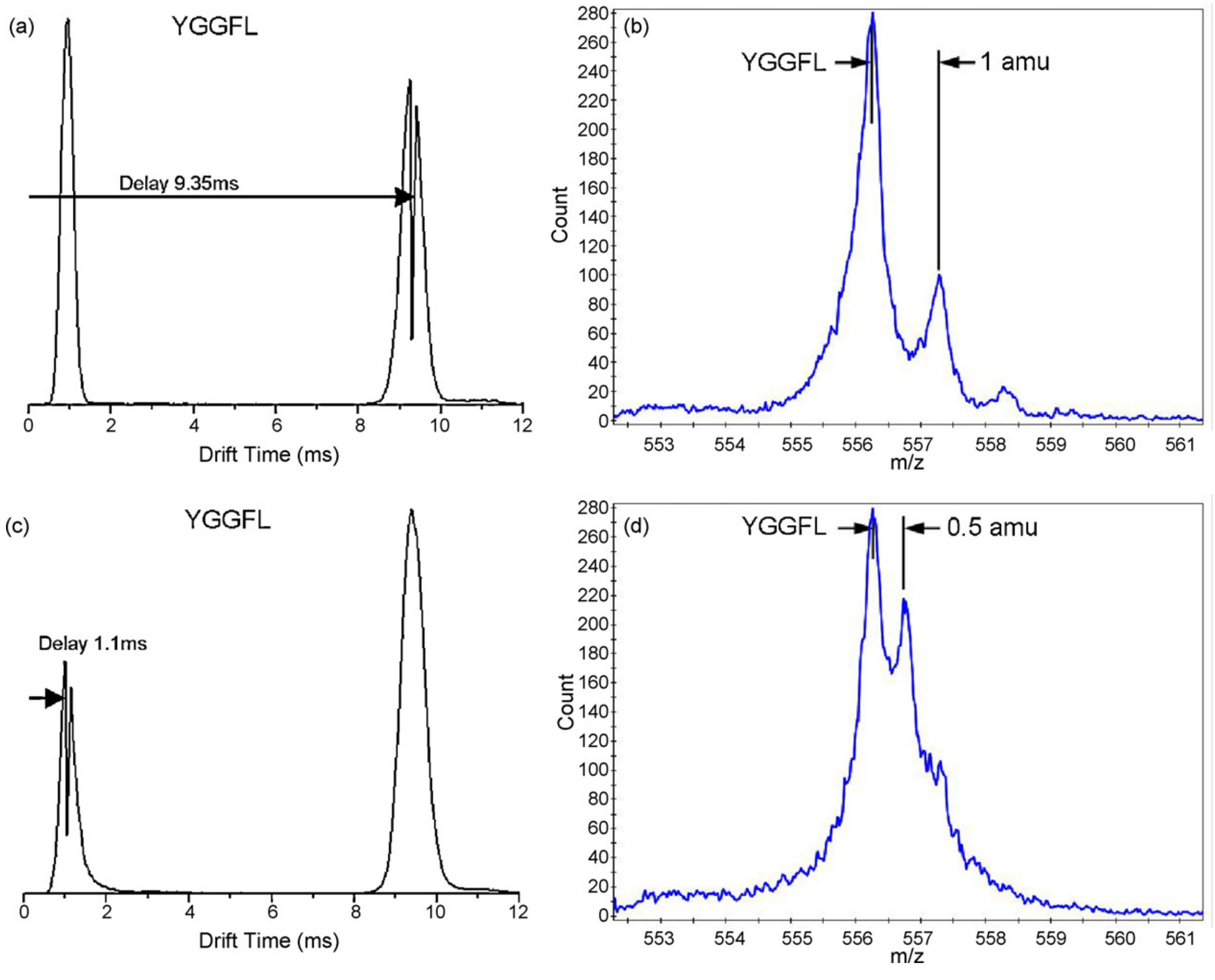

**Fig. 8.** (a) ATD of leucine-enkephalin [YGGFL]$^{+1}$ showing "slice" of long time feature (at 9.35 ms) selected by the TOF; (b) TOFMS of this ATD feature; (c) TOF selection of short time ATD feature (at 1.1 ms); (d) TOFMS of this faster feature. The drift times scale is not indicative of the total drift time and is present to show the time separation of the two features.

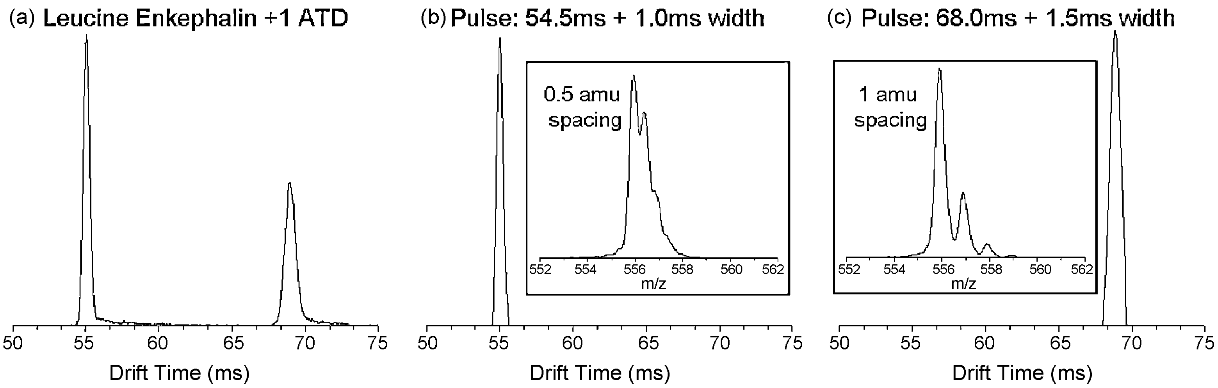

**Fig. 9.** (a) ATD of Leu-enkephalin [YGGFL]$^{+1}$; (b) ATD feature at 55 ms selected using the pre-quadrupole lenses. Inset shows the quadrupole mass spectrum of this 55 ms ATD feature. The 0.5 amu $^{13}$C spacing shows that this is a doubly charged dimer ion; (c) Corresponding amu of 69 ms feature. The 1.0 amu spacing of the $^{13}$C peaks in the insert shows that this species is a singly charged monomer.

the mobility and TOF MS parts of the experiment are done separately. Because the ion drift time is typically 50–100 ms, a maximum (non-interleaved) experimental repetition rate less than 10–20 Hz must be used in these mobility measurements. In contrast, when the TOFMS measurements are done separately, a repetition period which corresponds to the width of the IMS features can be used. These are typically 3–5 ms which corresponds to a repetition rate >200 Hz. Thus the TOF acquisition speed is enhanced by an order of magnitude relative to that possible when the absolute mobility is measured at the same time. Since the (low repetition rate) mobility measurements are done with the QMS detector where intensities are far greater than the TOFMS signal levels, dividing the experiment this way is more efficient.

Fig. 8 shows an experiment in which two individual ATD peaks of the +1 charge state of leucine-enkephalin (YGGFL, $m/z = 556.6$) are recorded while the TOFMS of an individual peak is recorded concurrently. Fig. 8(a) shows the ATD peaks with a “slice” taken out of the slower peak by the TOF extraction. The resulting TOFMS is shown in Fig. 8(b). The 1 amu $^{13}$C spacing shows that this IMS peak is the +1 monomer. The corresponding results for the first ATD peak are shown in Fig. 8(c) and (d). Here, the $^{13}$C spacing is 0.5 amu and the IMS peak must be due to the +2 dimer ion. The short ATD time base in this experiment is due to the high repetition rate discussed above.

In practice, the TOF resolution is currently limited by collisions with stray bath gas molecules and better pumping in this region is required to optimize resolution.

### 3.5. Quadrupole MS of selected ATD peak

Much the same experiment (mass spectrum of a selected ATD peak) can be done by selectively gating the ions that comprise a particular ATD feature and scanning the quadrupole MS. This gating is done with the steering lenses before the quadrupole. This is illustrated in Fig. 9; where Fig. 9(a) again shows the two features in the ATD of leucine enkephalin [YGGFL]$^{+1}$ ($m/z = 556.6$). Fig. 9(b) shows the first ATD feature selected and its mass spectrum and Fig. 9(c) shows the selection of the second feature and its mass spectrum. Again, it can easily be seen that the slower ATD feature (at 69 ms) has a $^{13}$C spacing of 1 amu (i.e., that it is a singly charged monomer) while the faster ATD species (at 55 ms) has a $^{13}$C spacing of 0.5, indicating that it is a doubly charged dimer. For ions with $m/z$ less than 1000 the quadrupole mass resolution is sufficient to distinguish monomer, dimer and trimer species. The advantage of this technique is its sensitivity. The entire ATD feature can be selected and examined, as opposed to a small fraction with the TOF (see Fig. 8). The same high ion pulse repetition rate discussed above also can be applied here but in this particular experiment the arrival times correspond to the true drift times (i.e., a low repetition rate was used, in contrast to the results in Fig. 8).

### 3.6. Ion heating and annealing

By increasing the electric field strengths in the entrance funnel/trap, the relative populations of ATD features can be changed. This corresponds to increasing the injection energy in previous experiments [20]. Although the energy gain is difficult to quantify, this heating can help identify oligomer species by dissociating trimers (for example) into dimers and monomers. This experiment is illustrated in Fig. 10. Bradykinin ions of nominal charge state +1 ($(\mathrm{BK}+\mathrm{H})_n{}^{+n}$) are seen to have multiple ATD features under low field conditions (bottom panel). As the source funnel fields are increased, the higher mobility features collapse into the slowest peak (at 68 ms) which dramatically gains in intensity (upper panel). This effect is most easily explained by dissociation of the type

$$(\mathrm{BK}+\mathrm{H})_n{}^{+n} \rightarrow (\mathrm{BK}+\mathrm{H})_{n-1}{}^{+(n-1)} + (\mathrm{BK}+\mathrm{H})^+ \qquad (3)$$

In addition, the trimer and dimer peaks, which show multiple features at low funnel voltages, appear as single, broader peaks at high funnel voltages, indicating a scrambling of the structures of these aggregates as they are collisionally excited.

## 4. Applications

In this section we present experiments which illustrate the useful application of the above techniques on some previously studied chemical systems.

### 4.1. Differentiating inverse peptides

Structural isomers which are inverse peptides have identical masses and $^{13}$C populations and cannot be differentiated by mass spectrometry alone. They may have different cross sections, however, and their separation by IMS is possible. We have examined such a system, namely the H-SDGRG-OH and H-GRGDS-OH pair. The quadrupole mass spectrum of a 50–50 mix of the two peptides is shown in Fig. 11(a) while the ATDs of the +2 and +1 charge states appear in Fig. 11(b) and (c). The cross sections of the +2 charge state ions differ by ~2.8% and are nearly baseline resolved. The cross sections of the +1 state are ~1% different and are resolved but the signal to noise is poor due to the low intensity of the peak. Interestingly, the cross section of the SDGRG isomer is larger than the GRGDS in the +2 charge state but smaller in the +1 charge state. (The identity

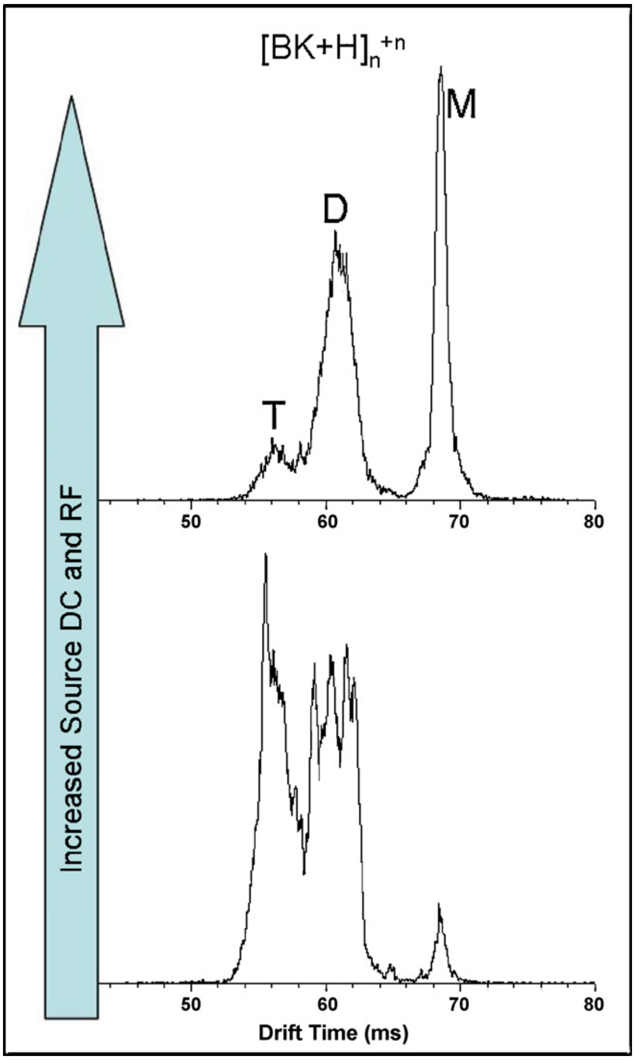

**Fig. 10.** Effect of heating on the $(BK+H)_n{}^{+n}$ ion. The ion energy is increased by increasing RF and DC field strengths in the entrance ion funnel. Note the dissociation of higher order oligomers into monomers as well as the blurring of the dimer and trimer structures (presumably due to interconversion of the vibrationally excited ions).

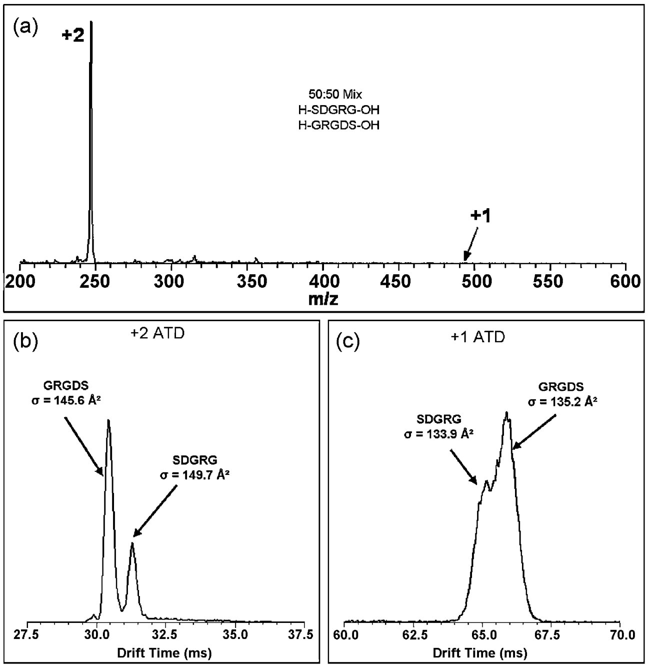

**Fig. 11.** Inverse peptides. (a) A quadrupole mass spectrum of a 50:50 mixture of the inverse peptides is shown. (b) ATD of the +2 charge state. The isomer cross sections differ by 2.8%; (c) ATD of +1 charge state. Here the cross sections are 1% different and reversed in order from the +2 charge state.

of the ATD peaks was established in separate experiments with the individual isomers.) Calculations are underway to help understand this reversal in size.

This system was investigated previously by Wu et al. [31]. Their instrumental resolution was insufficient to differentiate the two isomers in their +1 charge states. The +2 charge state cross sections were 5.2% different (in their experiment, using $N_2$ bath gas at a temperature of 250 °C).

### 4.2. *Differentiating optical isomers*

As in the case of inverse peptides, optical isomers cannot be distinguished by mass spectrometry alone. In order to gain insight into the effect of d-amino acid substitution on cross section, two substituted enkephalin peptides were examined. These were the [Tyr-dAla-Gly-Phe-Leu] and [Tyr-dAla-Gly-Phe-dLeu] molecules. The ATD resulting from the +1 charge state ($m/z = 570.7$) of the electro-sprayed [Tyr-dAla-Gly-Phe-Leu] sample is shown in Fig. 12(a). Two widely spaced peaks are present. Fig. 12(b) and (c) shows the individual mass spectra of the two species with the $^{13}C$ spacing clearly identifying them as the +1 monomer and +2 dimer. The ATD of the +1 charge state of the second enkephalin [Tyr-dAla-Gly-Phe-dLeu] is shown in Fig. 12(d); in this case the dimer population is near zero. The ATD of a 1:1 mixture of the two enkephalin species is given in Fig. 12(e). The cross sections of the two monomer species from the two isomeric samples are identical within experimental uncertainty (± 0.1%) and cannot be resolved. The dimer species do exhibit significantly different behavior, however. The hetero dimer has a cross section 1.5% less than the [Tyr-dAla-Gly-Phe-Leu] homo dimer. Thus, although the simple parent ions of these optical isomers are not resolvable with IMS, the corresponding dimers are.

This system was also examined by Wu et al. [31]. They measured a 0.4% difference in cross section between the two monomer species. No dimer species were observed. Again, their experiment used $N_2$ bath gas at 250 °C.

### 4.3. *Bradykinin structures*

Bradykinin and its protonated forms ($(BK+H)^{+1}$, $(BK+2H)^{+2}$ and $(BK+3H)^{+3}$) have been extensively studied with a number of experimental [32] and theoretical [33] articles appearing in the literature (see Ref. 33a and the references therein). There appears to be a consensus that the singly protonated molecule forms a salt bridge structure in the gas phase rather than a charge solvation form. This conclusion is based on calculations [33] showing the salt bridge form to be lower in energy as well as experimental black-body dissociation [32b,c] and IMS studies [20,32a,d,e]. The MALDI mass spectrum of bradykinin and the corresponding ATD spectrum of the sodiated parent $(BK+Na)^{+1}$ ($m/z = 1083$) are shown in Fig. 13. The sodiated parent ion shows at least three stable structures (lower panel) which were not resolved in lower resolution experiments (upper panel). The corresponding ESI results are given in Fig. 14 along with previous, lower resolution ATDs for comparison. The species in this ESI experiment are the protonated (not sodiated) peptides. It appears that here the monomer forms only one sta-

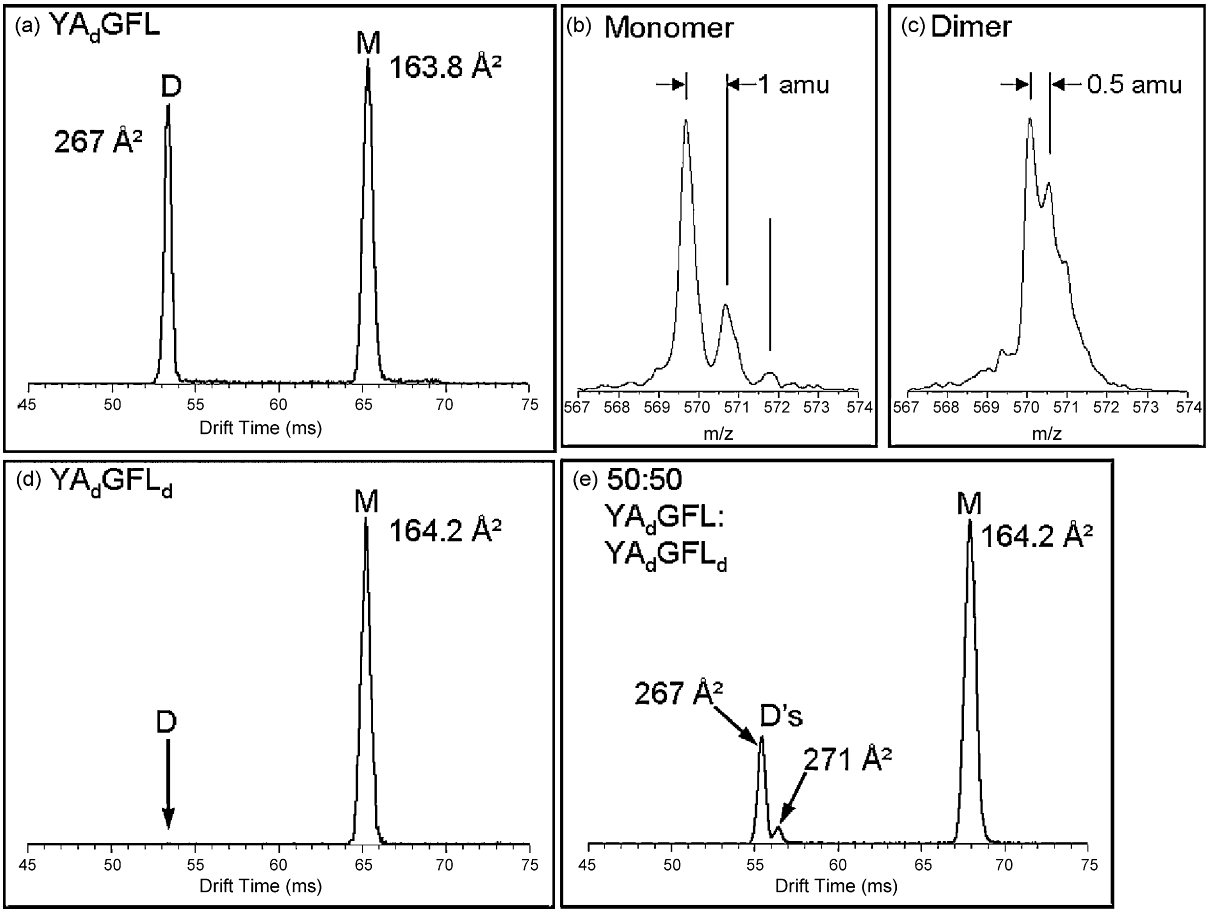

**Fig. 12.** Leu-Enkephalin optical isomers. (a) ATD of [Tyr-dAla-Gly-Phe-Leu]$^{+1}$ ion showing two species with widely different cross sections; (b) QMS of the 65 ms ATD peak in panel (a) where the 1 amu spacing shows the species is monomeric; (c) QMS of the 53 ms ATD peak in panel (a) where the 0.5 amu spacing shows it to be a doubly charged dimer. (d) ATD of [[Tyr-dAla-Gly-Phe-dLeu]$^{+1}$ ion showing almost no dimer. (e) ATD of 50:50 mix of the Leu-enkephalins from panels (a) and (d). The 68 ms peak is due to unresolved monomer +1 of both species. The 267 Å$^2$ cross section peak is due to the [Tyr-dAla-Gly-Phe-Leu]$_2^{+2}$ dimer while the 271 Å$^2$ peak is from the [Tyr-dAla-Gly-Phe-Leu]$^{+1}$-[Tyr-dAla-Gly-Phe-dLeu]$^{+1}$ hetero-dimer species.

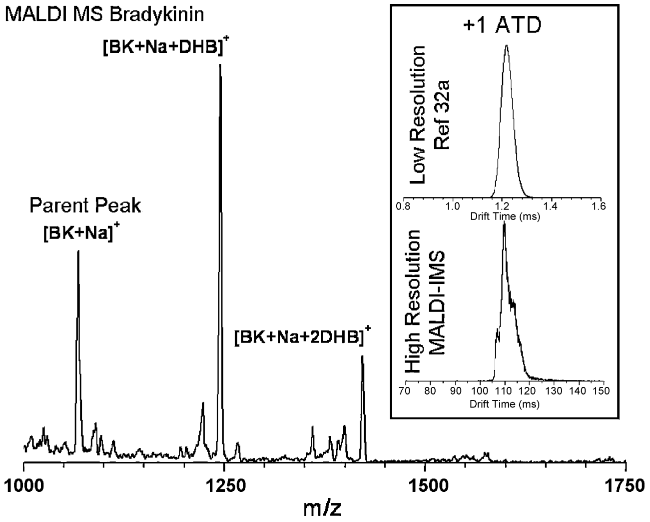

**Fig. 13.** Quadrupole mass spectrum of bradykinin ion formed by MALDI ion source. Note the DHB matrix adduct peaks. The inset shows the ATDs of the (BK + Na)$^{+1}$ ion. Note the presence of multiple configurations in the high resolution panel. The resolution of the MALDI experiment is lower than the corresponding ESI experiment (see text).

ble isomer. The differences in the MALDI and ESI results may be due to the protonated vs. sodiated species, the ionization technique or some other factor. The most likely three conformers in the (BK + Na)$^{+1}$ ATD are the charge solvated species and two salt bridged species with the carboxyl group deprotonated and Arg1 or Arg9 protonated. The protonated ion (BK + H)$^{+1}$ gives rise to a single monomer peak in the ATD of Fig. 14(a), consistent with a salt bridge structure being dominant.

Fig. 14(b) shows the (BK + 2H)$^{+2}$ ATD with two, well resolved structures. The $^{13}$C spacing (Fig. 6) shows that these are both monomer species. Previous high-resolution IMS, black-body dissociation studies [32b,c] and FAIMS studies [34] have also indicated the presence of two isomeric forms of this ion. Calculations find two low lying zwiterionic structures, with the lowest charge solvation structure about 7 kcal higher in energy [33a]. Fig. 14(d) shows the (BK + 3H)$^{+3}$ ATD where three monomeric isomers are seen. Here, calculations indicate the charge solvation form is lowest in energy but the presence of three stable structures is not yet understood.

It is also worth contrasting the ATD peaks of the dimer and trimer oligomers of the(BK + H)$_n^{+n}$ peak, ($m/z$ = 1061) with those reported previously (Fig. 14(a)). Where only one dimer and one trimer peak were apparent before, now at least three stable dimer and two trimer forms can be seen. Similarly, the +3/2 charge state ($m/z$ = 708.7), which must be a dimer, now shows three structures where only one was visible previously (Fig. 14(c)).

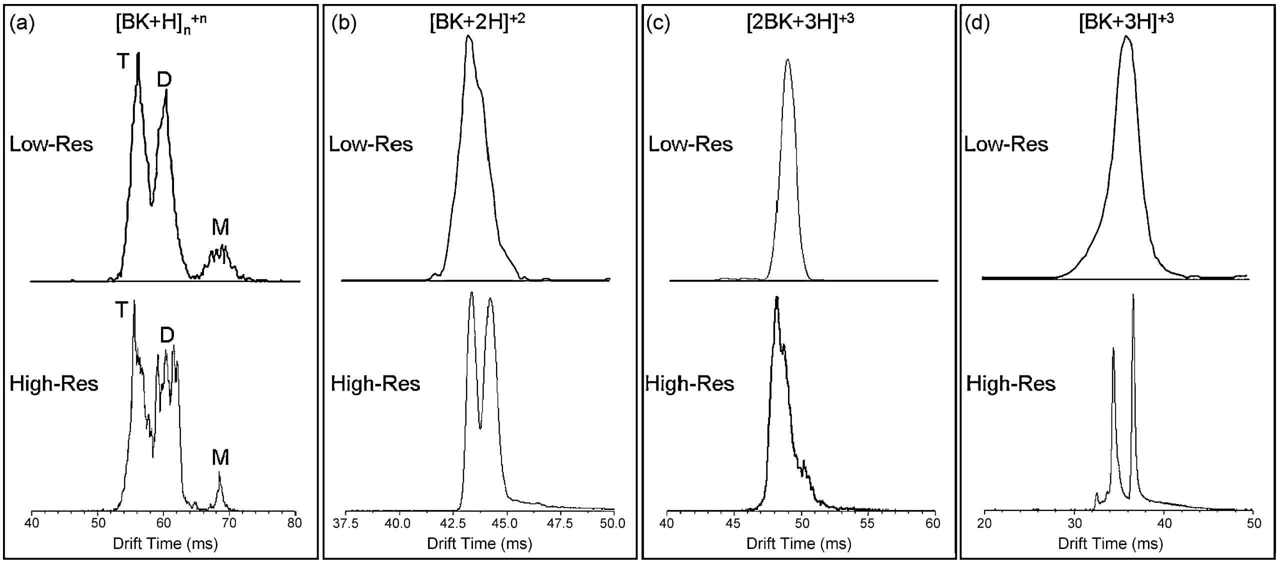

**Fig. 14.** High resolution IMS spectra of protonated bradykinin ions formed by ESI (the quadrupole MS of bradykinin is shown in Fig. 2). Previous, lower resolution spectra are shown above. (a) $z/n = +1$, (b) $z/n = +2$, (c) $z/n = +3/2$, (d) $z/n = +3$, where $z$ is the charge and $n$ is the aggregate number ($n = 1$ is monomer, $n = 2$ is dimer, etc.).

## 5. Summary

A new, high resolution MS/IMS instrument has been described. The design and performance of this instrument has been optimized for the purpose of separating conformers with similar mobilities, accurately measuring the absolute ion collision cross sections and identifying oligomeric species through $^{13}$C spacing. The drift tube and ion funnel arrangements have been adapted from other instruments which previously employed similar arrangements [17,18] and have been optimized to include a quadrupole mass analyzer. New physical design features on this instrument include the incorporation of an interchangeable electrospray and MALDI ion source as well as a quadrupole mass analyzer following the drift tube and prior to the time of flight analyzer. On this instrument arrival time distributions are measured on the quadrupole electron multiplier, where as, on instruments of similar design arrival time distributions are reconstructed from a series of TOF mass spectra [17,18]. The detection efficiency of the electron multiplier arrangement should me many times more sensitive than the TOF detection method. Performance features of this instrument include IMS resolution greater than 100 and the use of either quadrupole or time of flight mass analyzers to examine a particular IMS feature. Finally several sets of illustrative experiments are described including a reexamination of the bradykinin peptide in various charge states, all of which show the presence of several stable isomeric forms. Resolution at the level available in this instrument will clearly be helpful in understanding the structural characteristics of biological molecules and other molecular species.

## Acknowledgements

This work is supported by the Air Force Office of Scientific Research under grants FA9550-05-1-0208 and FA9550-06-1-0069. Partial support from the National Science Foundation under grant CHE-0503728 is also gratefully acknowledged.

## References

[1] G. von Helden, M.-T. Hsu, P.R. Kemper, M.T. Bowers, J. Chem. Phys. 95 (1991) 3835.
[2] M.T. Bowers, P.R. Kemper, G. von Helden, P.A.M. van Koppen, Science 260 (1993) 1446.
[3] (a) G. von Helden, T. Wyttenbach, M.T. Bowers, Science 267 (1995) 1483;
(b) G. von Helden, T. Wyttenbach, M.T. Bowers, Int. J. Mass Spectrom. Ion Process. 146 (1995) 349.
[4] D.E. Clemmer, M.F. Jarrold, J. Mass Spectrom. 32 (1997) 577.
[5] T. Wyttenbach, M.T. Bowers, Top. Curr. Chem. 225 (2003) 207.
[6] (a) P. Weis, P.R. Kemper, M.T. Bowers, J. Phys. Chem. A 101 (1997) 8207;
(b) T. Wyttenbach, G. von Helden, M.T. Bowers, Int. J. Mass Spectrom. Ion Process. 165 (1997) 377;
(c) S. Lee, T. Wyttenbach, M.T. Bowers, Int. J. Mass Spectrom. Ion Process. 167 (1997) 605.
[7] (a) T. Wyttenbach, G. von Helden, J.J. Batka, D. Carlat, M.T. Bowers, J. Am. Soc. Mass Spectrom. 8 (1997) 275;
(b) M.F. Mesleh, J.M. Hunter, A.A. Shvartsburg, G.C. Schatz, M.F. Jarrold, J. Phys. Chem. 100 (1996) 16082;
(c) A.A. Shvartsburg, M.F. Jarrold, Chem. Phys. Lett. 261 (1996) 86.
[8] M.J. Manard, P.R. Kemper, M.T. Bowers, Int. J. Mass Spectrom. 249–250 (2006) 252.
[9] (a) J. Gidden, T. Wyttenbach, J.J. Batka, P. Weis, A.T. Jackson, J.H. Scrivens, M.T. Bowers, J. Am. Chem. Soc. 121 (1999) 1421;
(b) J. Gidden, T. Wyttenbach, J.J. Batka, P. Weis, A.T. Jackson, J.H. Scrivens, M.T. Bowers, J. Am. Chem. Soc. 122 (2000) 4692;
(c) M.A. Summers, P.R. Kemper, J.E. Bushnell, M.R. Robinson, G.C. Bazan, M.T. Bowers, S.K. Buratto, J. Am. Chem. Soc. 125 (2003) 3341;
(d) S.E. Anderson, C. Mitchell, T.S. Haddad, V. Aij, J.J. Schwab, M.T. Bowers, Chem. Mater. 18 (2006) 1490.
[10] (a) J. Gidden, J.E. Bushnell, M.T. Bowers, J. Am. Chem. Soc. 123 (2001) 5610;
(b) J. Gidden, A. Ferzoco, E.S. Baker, M.T. Bowers, J. Am. Chem. Soc. 126 (2004) 15132;
(c) J. Gidden, E.S. Baker, A. Ferzoco, M.T. Bowers, Int. J. Mass Spectrom. 240 (2005) 183;
(d) V. Gabelica, E.S. Baker, M.-P. Teulade-Fichou, E. DePauw, M.T. Bowers, J. Am. Chem. Soc. 129 (2007) 895;
(e) C.S. Hoaglund, Y. Liu, A.D. Ellington, M. Pagel, D.E. Clemmer, J. Am. Chem. Soc. 119 (1997) 9051.
[11] (a) T. Wyttenbach, J.E. Bushnell, M.T. Bowers, J. Am. Chem. Soc. 120 (1998) 5098;
(b) T. Wyttenbach, J.J. Batka, J. Gidden, M.T. Bowers, Int. J. Mass Spectrom. Ion Process. 193 (1999) 143;
(c) T. Wyttenbach, M. Witt, M.T. Bowers, J. Am. Chem. Soc. 122 (2000) 3458;
(d) S.L. Bernstein, T. Wyttenbach, A. Baumketner, J.-E. Shea, G. Bitan, D.B. Teplow, M.T. Bowers, J. Am. Chem. Soc. 127 (2005) 2075;
(e) A. Baumketner, S.L. Bernstein, T. Wyttenbach, G. Bitan, D.B. Teplow, M.T. Bowers, J.-E. Shea, Protein Sci. 15 (2006) 420;
(f) K.B. Shelimov, M.F. Jarrold, J. Am. Chem. Soc. 118 (1996) 10313;
(g) K.B. Shelimov, D.E. Clemmer, R.R. Hudgins, M.F. Jarrold, J. Am. Chem. Soc. 119 (1997) 2240;
(h) R.R. Hudgins, M.A. Ratner, M.F. Jarrold, J. Am. Chem. Soc. 120 (1998) 12974.
[12] B.M. Kolakowski, Z. Mester, Analyst 132 (2007) 842.
[13] Y.Z. Guo, J.X. Wang, G. Javahery, B.A. Thomson, K.W.M. Siu, Anal. Chem. 77 (2005) 266.
[14] S.D. Pringle, K. Giles, J.L. Wildgoose, J.P. Williams, S.E. Slade, K. Thalassinos, R.H. Bateman, M.T. Bowers, J.H. Scrivens, Int. J. Mass Spectrom. 261 (2007) 1.
[15] S.J. Valentine, A.E. Counterman, C.S. Hoaglund, J.P. Reilly, D.E. Clemmer, J. Am. Soc. Mass Spectrom. 9 (1998) 1213.

[16] S.C. Henderson, S.J. Valentine, A.E. Counterman, D.E. Clemmer, Anal. Chem. 71 (1999) 291.

[17] E.S. Baker, B.H. Clowers, F. Li, K. Tang, A.V. Tolmachev, C.C. Prior, M.E. Belov, R.D. Smith, J. Am. Soc. Mass Spectrom. 18 (2007) 1176.

[18] S.L. Koeniger, S.I. Merenbloom, S.J. Valentine, M.F. Jarrold, H.R. Udseth, R.D. Smith, D.E. Clemmer, Anal. Chem. 78 (2006) 4161.

[19] S.A. Shaffer, K. Tang, G.A. Anderson, D.C. Prior, H.R. Udseth, R.D. Smith, Rapid Commun. Mass Spectrom. 11 (1997) 1813.

[20] T. Wyttenbach, P.R. Kemper, M.T. Bowers, Int. J. Mass Spectrom. 212 (2001) 13.

[21] K. Tang, A.A. Shvartsburg, H.N. Lee, C.C. Prior, M.A. Buschbach, F.M. Li, A.V. Tolmachev, G.A. Anderson, R.D. Smith, Anal. Chem. 77 (2005) 3330.

[22] Y. Ibrahim, K.Q. Tang, A.V. Tolmachev, A.A. Shvartsburg, R.D. Smith, J. Am. Soc. Mass Spectrom. 17 (2006) 1299.

[23] J.S. Page, B. Bogdanov, A.N. Vilkov, D.C. Prior, M.A. Buschbach, K. Tang, R.D. Smith, J. Am. Soc. Mass Spectrom. 76 (2005) 244.

[24] Lumanova Laser, GmbH, 30419, Hannover, Germany.

[25] SIMION, Idaho National Engineering Laboratory, Idaho Falls, ID 83415.

[26] Extrel CMS, Pittsburgh, PA15238-2838, USA.

[27] Ortec, Oak Ridge, TN 37830.

[28] R.M. Jones, S.L. Anderson, Rev. Sci. Instrum. 71 (2000) 4335.

[29] H.E. Rivercomb, E.A. Mason, Anal. Chem. 47 (1975) 970.

[30] W.F. Siems, C. Wu, E.E. Tarver, H.H. Hill, P.R. Larsen, D.G. McMinn, Anal. Chem. 66 (1999) 4195.

[31] C. Wu, W.F. Siems, J. Klasmeier, H.H. Hill, Anal. Chem. 72 (2000) 391.

[32] (a) T. Wyttenbach, G. von Helden, M.T. Bowers, J. Am. Chem. Soc. 118 (1996) 8355;
(b) P.D. Schnier, W.D. Price, R.A. Jockusch, E.R. Williams, J. Am. Chem. Soc. 118 (1996) 7178;
(c) W.D. Price, P.D. Schnier, E.R. Williams, Anal. Chem. 68 (1996) 859;
(d) A.E. Countermann, S.J. Valentine, C.A. Srebalus, S.C. Henderson, C.S. Hoaglund, D.E. Clemmer, J. Am. Soc. Mass Spectrom. 9 (1998) 743;
(e) T. Wyttenbach, M.T. Bowers, J. Am. Soc. Mass Spectrom. 10 (1999) 9;
(f) A.C. Gill, K.R. Jennings, T. Wyttenbach, M.T. Bowers, Int. J. Mass Spectrom. 195/196 (2000) 685;
(g) N.P. Ewing, G.A. Pallante, X. Zhang, C.J. Cassady, J. Mass Spectrom. 36 (2001) 875.

[33] (a) C.F. Rodriquez, G. Orlova, Y.Z. Guo, L. Xiaomao, C.-K. Siu, A.C. Hopkinson, K.W.M. Siu, J. Phys. Chem. B 110 (2006) 7528;
(b) E.F. Strittmatter, E.R. Williams, J. Phys. Chem. A 104 (2000) 6069.

[34] (a) R.W. Purves, D.A. Barnett, B. Ells, Rapid Commun. Mass Spectom. 15 (2001) 1453;
(b) A.A. Shvartsburg, F.M. Li, K.Q. Tang, Anal. Chem. 78 (2006) 3706.

[35] P. Dugourd, R.R. Hudgins, D.E. Clemmer, M.F. Jarrold, Rev. Sci. Instrum. 68 (1997) 1122.